A New Concept for a Flat Lens Design Using Dielectric Cylinders

Eran Falek, *Student Member, IEEE*, and Reuven Shavit, *Senior Member, IEEE*

***Abstract*— A new design method called the array scattering method for a flat lens made of dielectric cylinders is presented. The method reconstructs the far-field radiation pattern of a 2-D arbitrary geometrical shape dielectric scatterer. Since the method has no restrictions on the near field, it allows us to alter the polarization currents distribution in order to obtain a better far-field performance for a periodic structure with a given unit cell size. The method also allows us to perform a simple parametric study on the limits of the unit cell size, taking into account the scatterer geometrical dimensions. This parameter (unit cell size) does not appear in the formulation if we use a method that assumes an infinite array of cylinders. The realization is done using the multiple scattering method, which is one of the most accurate methods to deal with arrays scattering. Nevertheless, the method is almost entirely analytic, not iterative and does not require multiple simulations in order to obtain the required objective.**

***Index Terms*— Artificial dielectrics, dielectric cylinders array, flat lens, homogenization, multiple scattering method (MSM).**

I. Introduction

Lenses are devices, which transform a plane wave (PW) to a spherical or a cylindrical wave (CW), and vice versa. In the optical regime, they are mainly used for magnifying, holography, and imaging. In the microwave regime, the main purpose of a lens is to enhance the directivity of an antenna. Conventional lenses are usually made of a material with constant permittivity. The contour of the lens (could be a sphere, cylinder, paraboloid, and so on) determines the focal point location.

Since the conventional lens is a large structure with somewhat complicated geometry, for some applications, a flat lens would be more appropriate. A flat lens has a simple structure of a rectangular bulk. There are some approaches for the design of a flat lens. The most commonly used are Fresnel lenses [1], transmission line metamaterials [2], zero index of refraction design [3], negative index of refraction [4], metasurfaces [5], and transformation optics (TrO) [6]. In this paper, we concentrate on TrO methods.

The TrO theory is based on the coordinate invariance of Maxwell's equations (see [7], [8]). This allows for controlling the wave paths inside a given device by distorting the spatial coordinates. The Jacobian of the coordinate transformation is absorbed in the new media permittivity and permeability, which becomes anisotropic and inhomogeneous. For these reasons, such devices are very hard to realize. However, Tang *et al.* [9] have shown that if the discrete coordinates in the physical space are near orthogonal, and the corresponding virtual space coordinates are strictly orthogonal, the lens is all dielectrics and is very close to be isotropic. This gives rise to the possibility to realize the lens using artificial dielectrics.

The concept of artificial dielectric materials is a relatively old concept. It was first proposed by Kock [1] to design a Fresnel lens. Kock made an artificial dielectric lens, which is made of metal plates. In 1958, it was shown by Brown [10] that dielectric materials can exhibit effective refractive index of less than unity. Since then, countless dielectric devices were designed for various applications (see [11]–[13]).

The realization of an artificial dielectric material is normally done using homogenization techniques. The most common homogenization method is the Lorenz theory (see [14]), which is a quasi-static method. More general methods, which do not assume quasi-static approximations, were presented in [15] and [16]. More accurate methods for complex particle geometries, based on full wave simulations and integral equations, also exist (see [17], [18]). For 2-D lenses implemented by periodic structures, it is convenient to use dielectric or conducting cylinders in the unit cell. Homogenization techniques for thin wire medium also exist in the literature (see [19]).

The common feature of the homogenization methods is that they all assume that the unit cell lies in an infinite array of identical particles. Under this assumption, it is impossible to account for the effect of the slab's size on the required unit cell size. While the methods proved to be useful for many large-scale applications, for relatively small slabs, such as flat lens for example, the unit cell has to be very small in order to obtain good agreement between the realized and the theoretical design. How small is usually determined by simulations. Another feature of homogenization is that we assume a polarization current density, which is a macroscopic quantity, and implement a discrete microscopic model. In other words, we design the near field of the lens and expect the far field to behave accordingly. However, for a radiation directivity enhancer, the far field is the important factor and not the near field.

The proposed array scattering method (ASM) is a new design method for 2-D artificial dielectric flat lenses made of thin dielectric cylinders. It is actually not a homogenization method in the sense that the polarization currents on the

Manuscript received January 23, 2017; revised August 22, 2017; accepted August 26, 2017. Date of publication September 15, 2017; date of current version October 27, 2017. *(Corresponding author: Eran Falek.)*

The authors are with the Department of Electrical and Computer Engineering, Ben-Gurion University of the Negev, Beer-Sheva 84105, Israel (e-mail: faleke@post.bgu.ac.il).

Color versions of one or more of the figures in this paper are available online at http://ieeexplore.ieee.org.

Digital Object Identifier 10.1109/TAP.2017.2752241

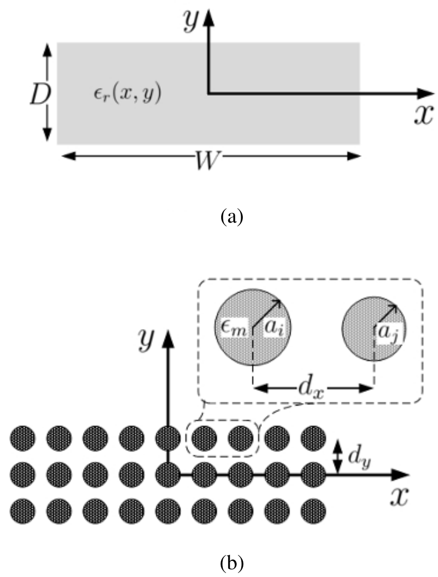

Fig. 1. (a) Model of a flat lens. An inhomogeneous dielectric slab, infinite in the z-directions, with dimensions of $W \times D$ in the xy plane. (b) Realized lens. An array of dielectric cylinders with relative permittivity ϵ_m with interelement spacing of $d_x \times d_y$. The radius of each cylinder is different and denoted by a_i for the ith cylinder.

cylinders correspond to the polarization current density of a continuous bulk slab. Instead, it is a far-field reconstruction method. The polarization currents on the cylinders are chosen such that the far field of the finite array emulates the far field of the continuous lens. Since an ASM is not a homogenization technique, the standard limitation on the unit cell size, i.e., $d \ll \lambda_g$, does not apply to it and therefore can be violated. The design is performed using the multiple scattering method (MSM) [20]. In this method, we calculate the scattered field of a scatterer in the vicinity of other scatterers, including the coupling effects. A parametric study on the limits of the unit cell size, which also considers the slab's thickness, is also conducted. The strength of the method is demonstrated by designing a flat lens and comparing its performance to similar lenses designed using standard homogenization methods.

This paper is arranged as follows. In Section II, we present the ASM. In Section III, we discuss the process of setting the target polarization currents on the cylinders by the use of filtering. In Section IV, we perform a parametric study on the effects of the unit cell size and the cylinder material permittivity. In Section V, we use the method to design a flat lens and further emphasize the advantage of this method over conventional homogenization techniques. Finally, in Section VI, we draw some conclusions.

II. Array Scattering Method

In this section, we present a new method called the ASM for a far-field reconstruction of a given structure using an array of dielectric cylinders. For simplicity, we consider a dielectric inhomogeneous slab, infinite in the z-direction with dimensions $W \times D$ in the xy plane, as shown in Fig. 1(a). The slab is excited by a known source with TE_z or TM_z polarization. In the following, we will consider the TM_z case. The realized lens is designed for this specific excitation. This is not a limitation, since the main application of this method is radiation enhancement for antennas. The antenna we wish to enhance has a known electric field distribution without the lens. This structure will be realized using an array of dielectric cylinders, as shown in Fig. 1(b). Since the cylinders are very thin, the interactions with electric fields pointing in the x- and y-directions are very weak, and therefore not in our scope of interest. The cylinders have relative permittivity ϵ_m, and the element spacing is d_x and d_y in the x- and y-directions, respectively. Each of the cylinders has a different radius. The radius of the ith cylinder is denoted by a_i. The difference in the radii allows the effective permittivity of the structure to vary as a function of the spatial coordinates.

A. Obtaining the Target Polarization Currents for the Cylinders

The ASM has three steps in the design. The first step is to calculate the exact total electric field in the slab in the case of the original continuous bulk slab. In some very simple cases, this can be done analytically, but in most cases, a numerical method has to be applied. The recommended method is the method of moments [21], since the results are obtained in terms of the polarization current density. However, different methods, such as the finite-element method (FEM), can be used as well. This step can also be performed using a commercial software, such as HFSS or CST. The excitation in this step is the exact excitation that will be applied on the realized slab. In this paper, we used either a PW or a CW excitation. But in the general case, one can calculate numerically the field of any type of feed. The second step is to obtain the polarization currents we wish to impose on the cylinders. Once the total electric field is calculated, we extract the continuous polarization current distribution from it with

$$J_p(x,y) = \begin{cases} j\dfrac{k_0}{\eta_0}(\epsilon_r(x,y)-1)E_z(x,y), & -\dfrac{W}{2} < x < \dfrac{W}{2} \\ & -\dfrac{D}{2} < y < \dfrac{D}{2} \\ 0, & \text{elsewhere} \end{cases} \tag{1}$$

where $k_0 = \omega/c_0$ is the vacuum wavenumber and $\eta_0 = \sqrt{\mu_0/\epsilon_0} = 120\pi$ is the vacuum wave impedance. This polarization current distribution is now sampled in the locations of the cylinders. If we choose to sample with a brute force approach, the sampling period d_x and d_y has to be determined so that the aliasing field in the visible region of the spectrum is beneath a certain threshold. This is a very important part of the design. As will be shown later, the decision on the unit cell size depends on the effective permittivity, the relative permittivity of the cylinders, and also on the slab's dimensions. The dependence on the bulk slab's size cannot be noticed unless we approach the realization as a sampling problem in a finite structure. Moreover, we can decrease the required sampling period by using antialiasing filters. This will be discussed in detail in Section III. For simplicity, for the rest of this paper, we use square unit cells, i.e., $d_x = d_y = d$.

The generalization to a rectangular unit cell is trivial. The third step in the design is to extract the radii of the cylinders using the MSM, as described in Section II-B.

B. Extracting the Cylinders Radii

At this point, we have determined the target polarization currents we wish to impose on the cylinders. Next, we use the MSM (see [20]) in order to extract the radius of each cylinder. Using the MSM, the incident field upon each cylinder is equal to the superposition of the scattering from all neighboring cylinders and the incident field. The MSM was chosen, since it can handle finite arrays of an arbitrary layout while taking into account the mutual coupling in an exact manner. However, for our purpose, we assume that the array is Cartesian with square unit cell (i.e., $d_x = d_y = d$). In general, the MSM can be applied to large-scale scatterers as well. For our purpose, it is safe to assume that the radius a_i of each cylinder is small enough such that only zero-order Hankel functions are needed to compute the scattered field. Accordingly, the scattered field of the ith cylinder is given by

$$E_{\mathrm{si}} = \upsilon_i H_0^{(2)}(k_0 \rho_i) \tag{2}$$

where $H_0^{(2)}$ stands for the zero-order Hankel function of the second kind, and $\rho_i = \sqrt{(x - x_i)^2 + (y - y_i)^2}$ is the distance between the cylinder and an observation point (x, y). υ_i is the CW harmonic amplitude. Let us define the free-space scattering operator $[\mathbf{S}]$ by

$$\upsilon_i = [\mathbf{S}]_{ij}\, \upsilon_j \tag{3}$$

where υ_i is the scattered field CW harmonic amplitude of the ith cylinder, and υ_j is the cylindrical harmonic amplitude of the jth cylinder. The scattered field of a cylinder located at the origin with radius a, illuminated by a unit magnitude incident TM_z PW, is given by [22]

$$E_z^{\mathrm{sc}} = -\sum_{n=0}^{\infty} j^{-n} R_n(a, \epsilon_m) e^{-jnw} H_n^{(2)}(k_0 \rho) \tag{4}$$

where w is the angle from the x-axis of the incident field wave vector (can be complex), and $R_n(a, \epsilon_m)$ is given by

$$R_n(a, \epsilon_m) = \frac{k_0 J_n(k_m a) J_n'(k_0 a) - k_m J_n(k_0 a) J_n'(k_m a)}{k_0 J_n(k_m a) H_n^{(2)'}(k_0 a) - k_m H_n^{(2)}(k_0 a) J_n'(k_m a)} \tag{5}$$

where $k_0 = \omega/c$, $k_m = k_0\sqrt{\epsilon_m}$, J_n is the Bessel function of the first kind of order n, and $H_n^{(2)}$ is the Hankel function of the second kind of order n. Since our cylinders are small in diameter, we can assume that any incident field on the cylinder behaves as a local PW incident on the cylinder. The magnitude of this PW is the sampled actual incident field at the center of the cylinder. The scattering operator $[\mathbf{S}]$ accounts for the scattering harmonic as a result of neighboring cylinder's scattered field. If we consider the scattered field of the neighboring cylinder to be the incident field of the cylinder of interest, one can write the scattering operator $[\mathbf{S}]$ with

$$[\mathbf{S}]_{ij} = -R_0(a_i, \epsilon_m) H_0^{(2)}(k_0 \rho_{ij}) \tag{6}$$

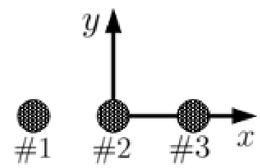

Fig. 2. Array of three cylinders with relative permittivity ϵ_m. The cylinders are given numbers for identification. The radius of $\#i$ is a_i.

where $\rho_{ij} = \sqrt{(x_i - x_j)^2 + (y_i - y_j)^2}$ is the distance between the cylinders. The next step in the formulation is to apply the scattering formula to an array. We derive the formulation here for a case of three scatterers, but the generalization to any number of scatterers is trivial. Consider an array of three dielectric cylinders with relative permittivity ϵ_m. The cylinders are given numbers for identification. Each cylinder has a radius of a_i according to the number of identification. The layout is shown in Fig. 2. The layout is shown to be on a straight line, but it does not have to be the case. The cylinders can be arranged in any arbitrary layout, where the center of the ith cylinder is located at $(x, y) = (x_i, y_i)$. The scattering operator has to be applied for each cylinder due to the field incident upon it. This field now consists the excitation incident field and the scattered field from the other cylinders. The CW harmonic amplitude of the cylinder #1 is given by

$$\upsilon_1 = [\mathbf{S}]_{12}\, \upsilon_2 + [\mathbf{S}]_{13}\, \upsilon_3 + [\mathbf{B}]_1\,. \tag{7}$$

The operator $[\mathbf{B}]_1$ gives the scattering spectrum of the first cylinder as a result from the incident exciting field. As discussed before, we can consider the incident field as a local PW with the magnitude of the sampled value at the center of the cylinder. In the general case, the operator $[\mathbf{B}]_i$ is given by

$$[\mathbf{B}]_i = -R_0(a_i, \epsilon_m) E_z^{\mathrm{inc}}(x_i, y_i), \quad i = 1, 2, 3. \tag{8}$$

The same can be written for all three cylinders, and thus we arrive to the matrix equation

$$\begin{pmatrix} \upsilon_1 \\ \upsilon_2 \\ \upsilon_3 \end{pmatrix} = \begin{pmatrix} 0 & [\mathbf{S}]_{12} & [\mathbf{S}]_{13} \\ [\mathbf{S}]_{21} & 0 & [\mathbf{S}]_{23} \\ [\mathbf{S}]_{31} & [\mathbf{S}]_{32} & 0 \end{pmatrix} \begin{pmatrix} \upsilon_1 \\ \upsilon_2 \\ \upsilon_3 \end{pmatrix} + \begin{pmatrix} [\mathbf{B}]_1 \\ [\mathbf{B}]_2 \\ [\mathbf{B}]_3 \end{pmatrix}. \tag{9}$$

Note that the operator $[\mathbf{S}]$ is symmetric with respect to i and j, i.e., $[\mathbf{S}]_{ij} = [\mathbf{S}]_{ji}$.

Up to this point, we derived what is called the *forward problem*. This actually means that given the layout of the scatterers, we can obtain the scattered fields. In this paper, we are interested in the *inverse problem*. The fields are known, and we are interested in the geometry. To this end, first, we derive the target CW harmonics on the cylinders. The scattered field by a single infinite line source is given by [22]

$$E_z^{\mathrm{scat}} = -\frac{k_0 \eta_0}{4} I H_0^{(2)}(k_0 \rho). \tag{10}$$

Thus

$$\upsilon_i^{\mathrm{target}} = -\frac{k_0 \eta_0}{4} I_i = -\frac{k_0 \eta_0}{4} J_p(x_i, y_i) d^2 \tag{11}$$

where $J_p(x_i, y_i)$ was defined in (1). In order to extract the radii of each cylinder, we write each equation in the matrix form (9) for the ith cylinder, assuming the other cylinders already achieved the target v_j^{target} in (11). The equation for the ith cylinder is, therefore

$$v_i = -R_0(a_i, \epsilon_m)\left[\sum_{j\neq i} H_0^{(2)}(k_0\rho_{ij})v_j^{\text{target}} + E_z^{\text{inc}}(x_i, y_i)\right]. \tag{12}$$

Equation (12) with the unknown radius a_i as a parameter in R_0 is a nonlinear equation. However, since R_0 is a known analytical function, we can extract a_i by demanding

$$a_i = \operatorname*{argmin}_{a_i}\left\{\left|v_i(a_i) - v_i^{\text{target}}\right|\right\}. \tag{13}$$

Using this method, we can emulate that the scattered field of any nonhomogenous dielectric object using dielectric cylinders as long as ϵ_m is high enough. However, the sampling rate required in order to achieve low errors in the far field can be quite high, and as a result, the unit cells have to be very small. In Section III, we encounter this problem by preprocessing the polarization currents prior to the radii extraction.

III. Preprocessing of the Polarization Currents and the Maximum Unit Cell Size

In this section, we concentrate on the sampling process of the polarization currents. First, we demonstrate the limits of a brute force sampling in terms of unit cell size. Then, we propose a preprocessing scheme, which allow us to use relatively large unit cells with good far-field results. We compare the new method with a conventional homogenization method based on the MSM, but assuming infinite array structure.

For the sake of simplicity, the demonstration of the concept is done on a slab with a constant ϵ_r, which is also infinite in the x-direction. The geometry is shown in Fig. 1. The excitation is a PW given by $\mathbf{E}^{\text{inc}} = \exp\{-jk_0y\}\hat{z}$. This is a good example, since the solution of the fields in the continuous case can be derived analytically. In fact, this is a 1-D problem, since the fields are constants in x. The total electric field inside the slab can be obtained using a simple transmission line theory to be

$$E_z = \frac{1+\Gamma_1}{1+\Gamma_2}e^{jk_0\frac{D}{2}}\left[e^{-jk_0n\left(y+\frac{D}{2}\right)} + \Gamma_2 e^{jk_0n\left(y+\frac{D}{2}\right)}\right] \tag{14}$$

where

$$\Gamma_1 = \frac{Z-n}{Z+n};\quad Z = \frac{n + j\tan(k_0nD)}{1 + jn\tan(k_0nD)}$$
$$\Gamma_2 = \frac{n-1}{n+1}e^{-2jk_0nD}$$

and $n = \sqrt{\epsilon_r}$ is the refraction index. The polarization currents are obtained using (1) (with $W \to \infty$). In order to determine the minimum allowed sampling rate, one has to look at the spatial spectrum [Fourier transform (FT)] of the continuous polarization current distribution

$$\widetilde{J}_p(k_x, k_y) = \iint_{\infty}^{\infty} J_p(y)e^{-j(k_xx+k_yy)}dx\,dy. \tag{15}$$

The FT of (14) is clearly two shifted Dirac's delta functions, and since the distribution is windowed in the region $-D/2 < y < D/2$, the delta functions are convolved with a sinc function. Since J_p does not depend on x, the integral in x gives a Dirac's delta as well. The spectrum is therefore

$$\widetilde{J}_p(k_x, k_y) = A\left[B\,\text{sinc}\left(\frac{D}{2}(k_y - k_0n)\right) + C\,\text{sinc}\left(\frac{D}{2}(k_y + k_0n)\right)\right] \times \delta(k_x) \tag{16}$$

where

$$A = j\frac{k_0}{\eta_0}(\epsilon_r - 1)\frac{1+\Gamma_1}{1+\Gamma_2}De^{jk_0\frac{D}{2}}$$
$$B = e^{-\frac{jk_0nD}{2}}$$
$$C = \Gamma_2 e^{\frac{jk_0nD}{2}}.$$

Also, $\text{sinc}(x) = \sin(x)/x$. The far-field scattered field is given, up to a constant, by a FT of the polarization currents, when the wave numbers have to satisfy the dispersion relation $k_0^2 = k_x^2 + k_y^2$. $\delta(k_x)$ in (16) implies that $k_x = 0$ is the only wave vector relevant. This means that the far-field information is located at $k_y = \pm k_0$. Indeed, the far field of this problem consists of two PWs propagating in the $\pm y$ directions. It is also known that the far field of any current distribution is located on the Ewald's sphere (see [23]) of the currents spectrum. In a 2-D problem, we get a Ewald's cylinder. In our case, we have a 1-D problem such that the Ewald's sphere gives two points. Sampling the current distribution in space causes replicas of the spectrum in the spectral domain. Thus, the sampling rate can be taken such that the aliasing of the first replica in the visible range is under a certain threshold.

Fig. 3(a) shows the spectrum of the continuous polarization currents (blue line) compared with the spectrum of the current distribution sampled with period $d = 0.12\lambda_0$. The slab thickness is $D = 0.6\lambda_0$ and $\epsilon_r = 9$. In this sampling period, we have five layers of cylinders in the sampled media. Note the difference in Fig. 3(a) at $k_y = -k_0$. This is a significant error due to aliasing (see [24]). This means that the transmitted field, which contributes to the far field in the region $y > 0$, is different. If we take denser sampling, for example, nine layers with $d = \lambda_0/15$ as shown in Fig. 3(b), the aliasing error reduces. If the slab is infinite in the y-direction, then the sincs would be very narrow, and the sampling rate would approach the limit of $d = \lambda_0/(2n)$ or $\lambda_g/2$. We consider this size as the *Nyquist limit* of the unit cell size. The Nyquist limit shows that the unit cell size has to depend on the effective parameters we try to achieve. In addition, this example shows that there is another factor besides the effective refractive index that limits the unit cell size. If the width of the slab is small, the sinc functions get wider and the aliasing error increases. Therefore, the decision on the unit cell size also depends on the slab's thickness. To the best of our knowledge, this is a new result. In the above-mentioned example, the Nyquist limit is $d_N = \lambda_0/(2\sqrt{9}) = 0.16\lambda_0$. However, due to aliasing caused by the finite thickness of the slab, a unit cell size of $d = 0.12\lambda_0$ is still not sufficient. With this being said, homogenization techniques usually involve averaging of the fields in the unit cell. This is some sort of filtering of the spectrum of the

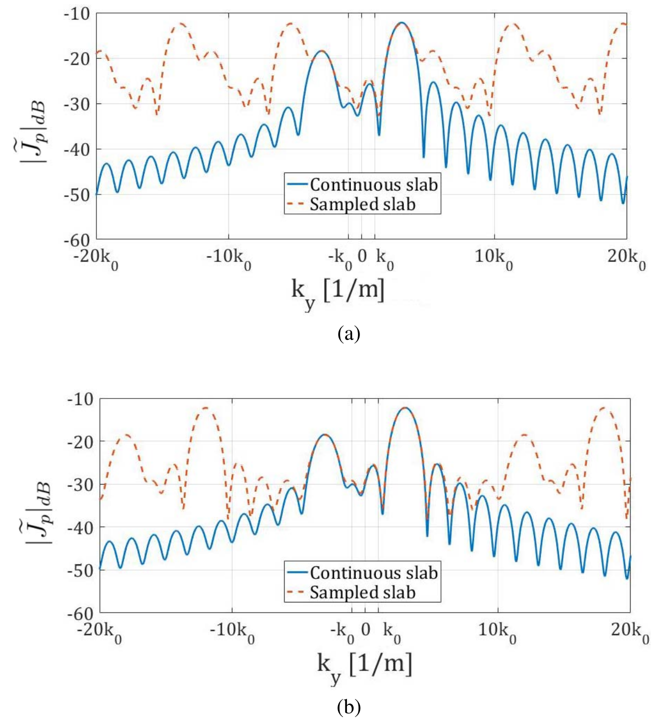

Fig. 3. (a) Spectrum of the polarization current distribution sampled with $d = 0.12\lambda_0$ (red dashed line) compared with the spectrum of the continuous current distribution of a slab with thickness $D = 0.6\lambda_0$ and $\epsilon_r = 9$. (b) Similar comparison with sampling period of $d = \lambda_0/15$.

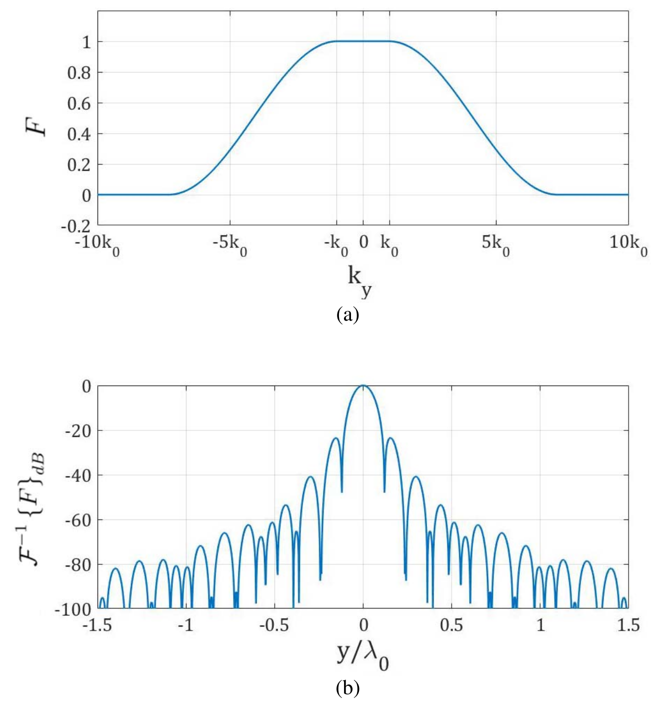

Fig. 4. (a) Filter used on the polarization current spectrum. (b) Inverse FT of the filter.

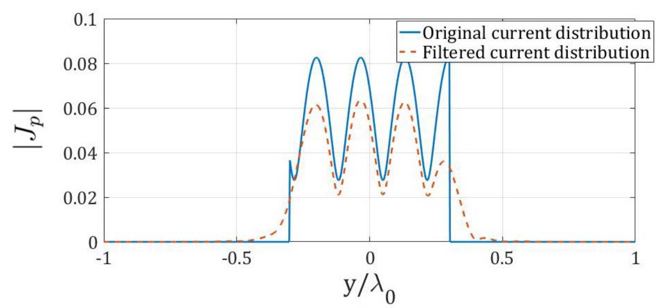

Fig. 5. Polarization current distribution on a slab with $D = 0.6\lambda_0$ and $\epsilon_r = 9$. The blue line is the original distribution. The red dashed line is the distribution after filtering. Note that the polarization current distribution after filtering is wider than the original due to the convolution with the filter.

currents, which means that the sampling rate can somewhat improve in comparison to the brute force example. However, it is very hard to quantify by how much.

The previous example also hints at the solution for reducing the sampling rate. If the reason behind the need for a small unit cell lies in the aliasing with the spectrum replicas, we can use an antialiasing filter in the spectral domain. The blue line in Fig. 3 shows the spatial currents spectrum of a slab with $D = 0.6\lambda_0$ and a permittivity of $\epsilon_r = 9$. One can notice that the sinc function peaks are located at $k_y = \pm k_0 n$. The width of the sinc functions is $4\pi/D$. When the currents are sampled, the spectrum will be duplicated for each $k_y = 2\pi m/d$, where $m \in \mathbb{Z}$. In order to avoid altering the visible spectrum, we apply a filter. Many types of filters can be applied. In this paper, we use a Hanning type window [25] for demonstration. The filter has to equal 1 all over the visible spectrum and vanish at $k_y^{\max} = 2\pi/d - k_0$. The filter function is therefore

$$F(k_y) = \begin{cases} 1, & |k_y| < k_0 \\ \dfrac{1}{2}\left[1 + \cos\left(\dfrac{\pi}{k_y^{\max} - k_0}(|k_y| - k_0)\right)\right], & |k_y| > k_0. \end{cases} \tag{17}$$

The filter in (17) is applied on the polarization currents spectrum $\widetilde{J}_p$. Then, by an inverse FT, we obtain a new polarization current distribution. The new polarization current distribution is wider than the original due to the convolution theorem. This means that the realized slab is thicker as well. As the sampling distance gets smaller, the width of the filter gets larger, and the addition to the realized slab decreases. In order to determine the new width of the slab, one has to analyze the FT of the filter we used. Fig. 4 shows the filter used in the example with $d = 0.12\lambda_0$ in the spectrum domain and its inverse FT (normalized). In Fig. 4(b), we see that the second lobe is already below -40 dB, and therefore, the filter effect beyond this point can be neglected. In this paper, we determine the slab's width by the first crossing point of -40 dB. The first y value, which reaches this value, is at $y = 0.21\lambda_0$. Therefore, after convolution, the slab will add about $0.21\lambda_0$ thickness on each side. This is shown in Fig. 5; note that the polarization currents are negligible beyond $y = D/2 + 0.21\lambda_0 = 0.51\lambda_0$. Fig. 6 shows the polarization current spectrum after applying the filter, compared to that of the continuous slab. One can see that the visible spectrum is not changed.

If the original slab is $0.6\lambda_0$ in thickness, and if the unit cell size is $d = 0.12\lambda_0$, we had a total of five layers of cylinders. In order to add $0.21\lambda_0$ thickness, it would be sufficient to add a single unit cell to each side. The actual thickness of the realized slab is the number of layers times the unit cell size. Here, the actual thickness is $0.84\lambda_0$ instead of $0.6\lambda_0$. In most cases, addition of a single layer to each side is quite sufficient.

At this point, we generated a new polarization current distribution. These polarization currents are sampled and become the target total currents ($I_i = J_p^{\text{new}}(x_i, y_i)d^2$) we wish to impose on the cylinders. The lowest possible sampling rate with filtering happens if the filter is a rectangular window over $|k_y| < k_0$. In this case, the unit cell size is $d = \lambda_0/2$ (which is above the Nyquist limit). However, in reality, this is not the case. While we can filter the currents spectrum for any sampling period, it is not clear whether we can realize the new distribution with the new method. Note that $R_0(a, \epsilon_m)$ in (5) is a complex function of a real variable a. We cannot necessarily set both real and imaginary parts to the desired value by changing a, and thus, the error in (13) can get quite large. However, as we get more layers, we have more degrees of freedom as we can affect the cylinders polarization currents using both the radius and the scattered field from the other cylinders. So as the number of layers increases (smaller unit cell), the error decreases. Also, the material of the cylinders affects R_0. Generally speaking, the effective permittivity is some sort of averaging between the host permittivity and the cylinders permittivity. Therefore, the permittivity of the cylinders has to be larger than the effective permittivity, and as ϵ_m increases, the cylinders radius decreases. If the cylinders' permittivity is close to the desired effective permittivity, the radii of the cylinders get larger. At a certain point, they will overlap, and the boundary conditions change. In the worst case, we get an entire slab made of ϵ_m, which means that we cannot control the effective permittivity at all. For these reasons, the radii of the cylinders are limited in this paper to $a_i \leq d/2$. In Section IV, we compare the ASM method with a standard homogenization method based on the MSM for the case of the infinite slab demonstrated earlier. This simplified problem can be solved rather fast with little computation resources, and thus is suitable for performing a comprehensive parametric study. After the parametric study, we can make the decisions on the choice of the number of layers for the realization, and the materials we use.

IV. Comparison of the ASM for Finite and Infinite Cases

In this section, we compare the performance of the new method with a conventional homogenization method, which assumes infinite array structure. Since the slab is infinite in the x-direction, the extraction method has to be further elaborated. The complete formulation for semi-infinite arrays can be found in Appendix A. This method will be referred to as the semi-infinite ASM. For comparison, we use a homogenization method based on the MSM as well. This method will be referred to as the infinite ASM. Although there are more efficient methods in terms of computational complexity (see [19]), the MSM results are the most accurate we can hope for as the method solves a full electrodynamic problem and considers all of the mutual coupling. Also, since all of the methods use the MSM, we can attribute the differences to the finiteness of the array. In the infinite array

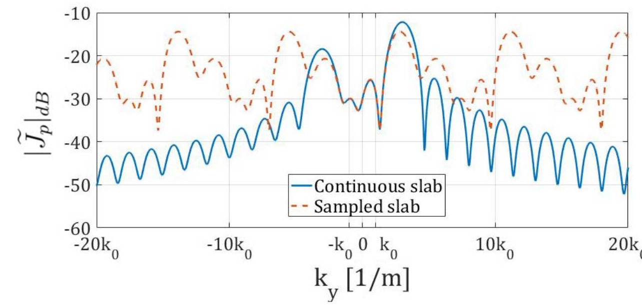

Fig. 6. Original polarization current distribution (blue line) against the filtered current distribution (red dashed line).

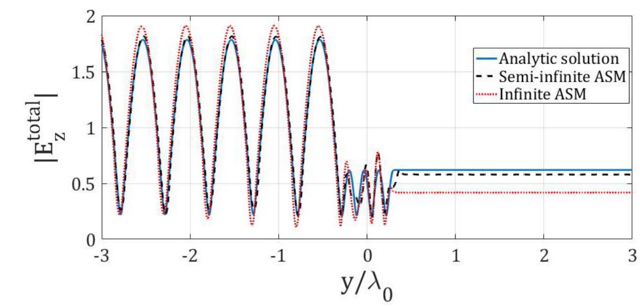

Fig. 7. Total electric field on the y-axis for a dielectric slab with $\epsilon_r = 9$, $D = 0.6\lambda$, infinite in the x-and z-directions, excited by a PW with TM_z polarization, and propagating in the y-direction. Blue line: analytical solution. Black dashed line: slab realized using the semi-infinite ASM. Red dotted line: slab realized using the infinite ASM. In both realizations, $\epsilon_m = 16$ and $d = 0.12\lambda_0$.

method, the polarization currents are obtained directly from the permittivity using (1) already in the sampled structure. In this case, we assume that the near field in the sampled structure behaves similar to that in the continuous slab. The averaged total field is calculated from these polarization currents to obtain a close-form formula from which we can extract the radii. The full formulation can be found in Appendix B. The infinite ASM is a standard homogenization method. Since the currents are obtained from the permittivity, and in our example, the permittivity is constant, the radius of all the cylinders is the same. Also, we can use cylinders only where the permittivity is larger than one. In the semi-infinite ASM, the polarization currents are obtained from the calculated total field. The sampled processed distribution does not necessarily satisfy (1). Thus, the far field will be accurate but the near field does not have to be. Also, as explained in Section III, the realized slab is wider than the original.

We compare the methods for a slab with $D = 0.6\lambda_0$, excited by a PW with electric field pointing in the z-direction and propagating in the y-direction. The slab's permittivity is $\epsilon_r = 9$. Fig. 7 shows the total electric fields on the y-axis. The field simulations were done using the FEM algorithm with the commercial software HFSS from ANSYS. The blue line represents the analytical field calculated for a continuous slab. The black dashed line is the field obtained with the semi-infinite ASM for $d = 0.12\lambda_0 = 0.36\lambda_g$. The red dotted line is the field obtained using the infinite ASM using the same unit cell size. Note that even though the unit cell dimensions

TABLE I
RADII OF THE CYLINDERS FOR A HOMOGENOUS SLAB DESIGNED WITH THE ASM

y_i/λ_0	a_i/λ_0 Semi-infinite ASM	a_i/λ_0 Infinite ASM
-0.36	0.0071	–
-0.24	0.0544	0.0468
-0.12	0.0470	0.0468
0	0.0507	0.0468
0.12	0.0480	0.0468
0.24	0.0429	0.0468
0.36	0.0159	–

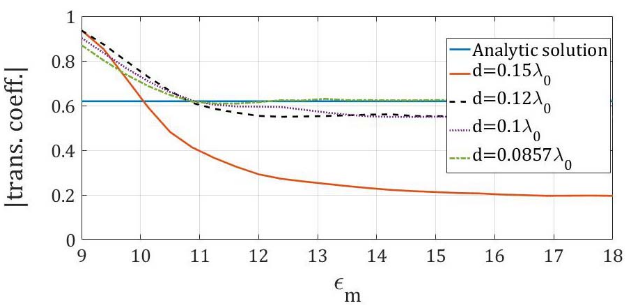

Fig. 8. Parametric study on a slab with $D = 0.6\lambda_0$ and $\epsilon_r = 9$. The blue line is the transmission coefficient calculated analytically. The other lines are the transmission coefficient of an array designed using the semi-infinite ASM as a function of the permittivity of the cylinders. The red line is for $d = 0.15\lambda_0$, black dashed line for $d = 0.12\lambda_0$, purple dotted line is for $d = 0.1\lambda_0$, and green dashed line for $d = 0.0857\lambda_0$.

stand within the Nyquist limit, there are substantial errors in the reflection and transmission field if we make the infinite array assumption to compute the dielectric cylinders radii. The material of the cylinders was chosen such that $\epsilon_m = 16$. Table I shows the radii and locations of the cylinders in the two designs. For the infinite ASM, we have five layers with the same radii. In the semi-infinite ASM, we have seven layers where the radius is different for each layer. The radius is different even though the slab's effective permittivity is constant. The change in the radius of the cylinders and the extra layers enable the improvement in the far field.

In order to make a decision on the materials we use for the cylinders, and the unit cell size (or alternatively, the number of layers), we can perform a parametric study on the simplified problem we demonstrated in this section. Fig. 8 shows the analytical calculation of the transmission coefficient (blue line) compared with the transmission coefficient of slabs realized with the semi-infinite ASM for different unit cell sizes and different permittivities. In the parametric study, we can see that a unit cell of $d = 0.15\lambda_0$ gives unacceptable results, but from $d = 0.12\lambda_0$ the error is reasonable. The graph reaches equilibrium at about $\epsilon_m = 14$. In the above-mentioned example, we chose $d = 0.12\lambda_0$ and $\epsilon_m = 16$. If the application requires higher accuracy, we can use lower sampling periods. This kind of test can be performed prior to designing any practical lens. The permittivity we test has to be the highest in the structure. From here, we can deduce the lowest possible permittivity in the material (higher permittivity usually go along with higher losses) and the unit cell size to use.

V. APPLICATION: FLAT LENS DESIGN WITH THE ASM

In this section, we implement the ASM in order to design flat lenses. A conventional 2-D lens is made of a material with constant permittivity and cylindrical contour (see [26]). The contour of the lens creates the focusing effect. Obtaining the same effect with a flat lens requires that the material is inhomogeneous. There are several methods to derive the permittivity function of the flat lens. In this paper, we use the TrO method. In particularly, we use the method in [9], since this method gives an isotropic and all-dielectric (i.e., $\mu_r = 1$) flat lens design. The main idea in the design is first to set the grid of the original homogeneous lens as close as possible to orthogonal. Then, the virtual space (i.e., the flat lens) is assigned with a strictly orthogonal grid. According to the results in [9], the permittivity in the virtual space is given by

$$\epsilon_r^{\text{lens}}(x', y') = \epsilon_r(x, y)\frac{S}{S'} \tag{18}$$

where S is the area of a surface element in the original space, and S' is the area of a surface element in the virtual space. For further details, see [9]. Fig. 9 compares the total electric fields of the three lenses excited by a PW with electric field pointing in the z-direction and propagating in the y-direction. One is a conventional lens with $\epsilon_r = 3$, $W = 4.44\lambda_0$, $D = 0.6\lambda_0$, and $D_m = 1.2\lambda_0$. The dimensions are described in Fig. 9(a). The second lens is the equivalent bulk flat lens with $W = 4.44\lambda_0$ and $D = 0.6\lambda_0$. The permittivity of the flat lens varies in the range $3 < \epsilon_r^{\text{flat}} < 6.08$. The third lens is the flat lens implemented with dielectric cylinders with $\epsilon_m = 16$ and a unit cell size of $d = 0.12\lambda_0$. The simulations in this section were performed with the FEM solver of the commercial software HFSS from ANSYS. Fig. 10 shows the complex magnitude of the total field on the y-axis for the three structures. The focal point of all three structures is located around $y = 4\lambda_0$. Since the maximum permittivity of the flat lens is higher, we have higher reflections, which explains the lower magnitude of the flat lenses at the focal point. Lower reflections can be obtained if both permittivity and permeability are computed according to TrO using the Jacobian. For practical reasons, we have decided to vary only the permittivity and accordingly, there is some degradation in the reflection level. This effect can be reduced by using matching layers at the input and output of the lens.

Next, we set a CW source at the focal point and calculate the far field of the structures. After performing a parametric study, we set the unit cell size on $d = 0.12\lambda_0$, which implies five layers in the y-direction, and after processing, we get seven layers. The cylinders have permittivity of $\epsilon_m = 16$. The far-field radiation pattern of the array is shown in Fig. 11 in red dotted line, compared with the far field of the conventional lens and the bulk flat lens in the blue and black dashed lines, respectively. The results are shown in the region $60° < \phi < 120°$, since beyond this angle the incident field does not interact with the lens. For comparison, the slab was also realized using the infinite ASM described in Appendix B. In this realization, we calculated in each unit cell the radius of the cylinder, assuming the cylinder lies in an infinite array of

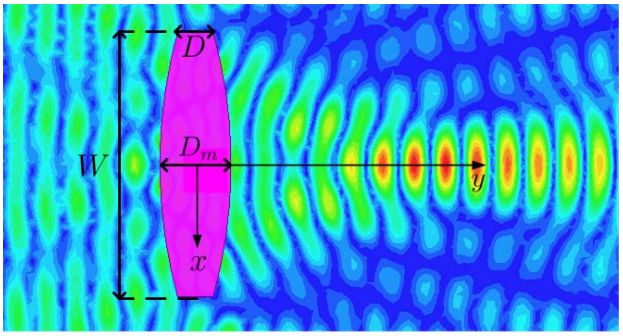

(a)

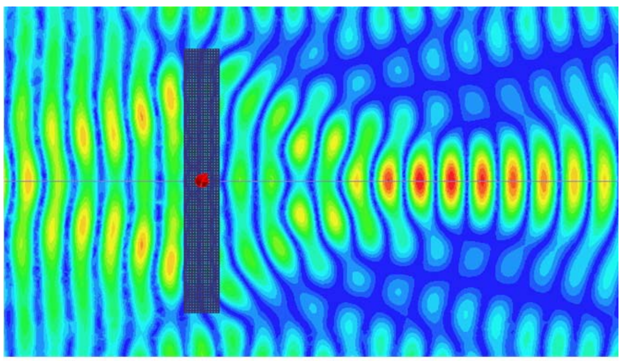

(b)

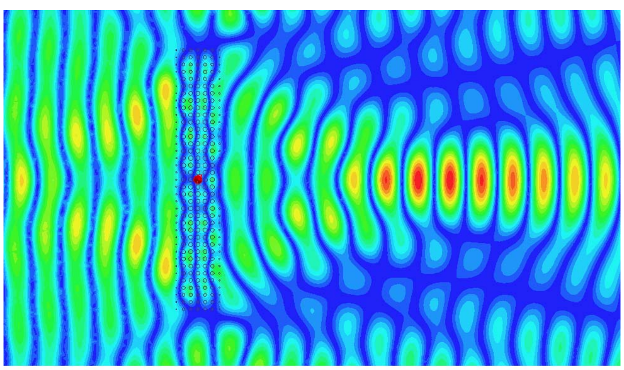

(c)

Fig. 9. Flat lens designs. (a) Real part of the total electric field of a conventional lens with $\epsilon_r = 3$, $W = 4.44\lambda_0$, $D = 0.6\lambda_0$, and $D_m = 1.2\lambda_0$. (b) Real part of the total electric field of the equivalent flat lens with $3 < \epsilon_r^{\text{flat}} < 6.08$. (c) Real part of the total electric field of a lens made of dielectric cylinders with $\epsilon_m = 16$ designed with the ASM. All of the lenses are excited by a PW with electric field pointing in the z-direction and propagating in the y-direction.

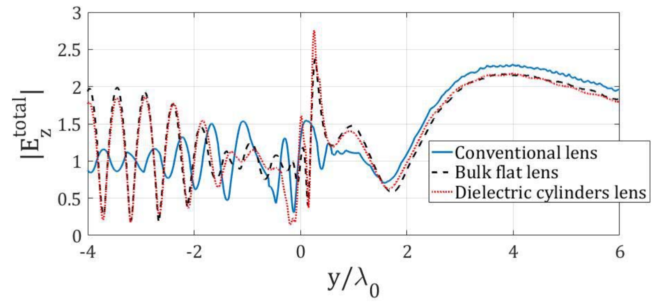

Fig. 10. Magnitude of the total electric field on the y-axis for the three lenses. The excitation is a PW $\mathbf{E}_i = \exp\{-jk_0 y\}\hat{z}$. The blue line is the conventional lens. The black dashed line is for the bulk flat lens, and the red dotted line is for the dielectric cylinders lens.

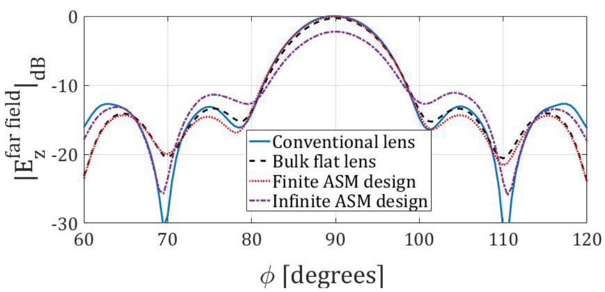

Fig. 11. Comparison of the far fields for different realization methods. The excitation is a line source located at the focal point $y = -4\lambda_0$. The blue line is the far field of the conventional lens. The black dashed line is for the bulk flat lens. The red dotted line is for an array of cylinders designed using the finite ASM. The purple dashed line is an array designed with the infinite ASM. The unit cell of the arrays designed using the ASM is $d = 0.12\lambda_0$, and the cylinders have relative permittivity of $\epsilon_m = 16$.

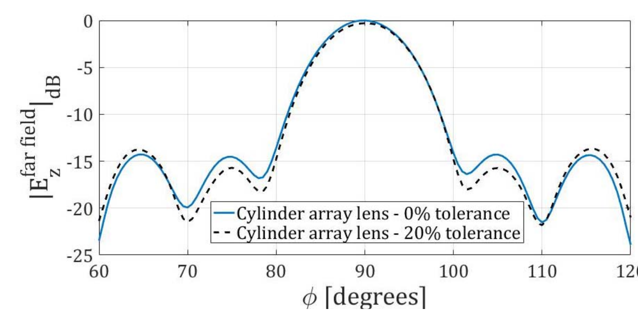

Fig. 12. Far-field radiation patterns of a cylinder array lens designed with the ASM with a tolerance of 0% in the radii compared with an array lens with 20% tolerance in the radii (statistical simulation). For each cylinder, the radius is a random variable with uniform distribution.

similar scatterers. The unit cell size and the cylinder's permittivity are the same as in the finite ASM design. The infinite ASM design is shown in Fig. 11 in purple dashed line. Even though we are not too close to the maximum unit cell size in terms of the Nyquist limit, we can see that the array designed by a method, which assumes infinite array design, falls short in comparison to the finite ASM. The first sidelobe is 2 dB higher than the bulk flat lens and 4 dB higher than in the finite ASM case. The main lobe of the infinite ASM is 2.5 dB lower than the other designs as well. The finite ASM design shows good agreement with the bulk flat lens and the conventional lens.

The method was formulated to fit any frequency band. However, it is clear that as we approach shorter wavelengths, the fabrication becomes very challenging. In these cases, variations in the radii of the cylinders are inevitable. Fig. 12 compares the far-field radiation patterns of two cylinder arrays. In the black dotted line we allowed a statistical perturbation of up to 20% in the radii of each cylinder compared to the original design shown in blue line. The result shown in Fig. 12 in black dotted line is a result of a single statistical simulation. It can be seen that the realization is stable for such variations.

The above-mentioned example shows that in the case of thin flat lenses, the finiteness of the array has to be a factor to consider. The finite ASM allows us to achieve good agreement with the bulk flat lens. If one wishes to use a standard homogenization method instead with the same agreement, he has to use smaller unit cells. The unit cell size and the material used for the cylinders can be determined using the simple parametric study shown in Section IV. This gives a complete design scheme for a flat lens.

VI. Conclusion

A new design method—the ASM—for 2-D inhomogeneous all dielectric slab realization using dielectric cylinders was suggested. The method is unique in that it does not assume that the array of cylinders is infinite for the computation of the cylinder's radius. This advantage has added value when flat lens is designed, since these lenses usually have low profiles. The method is based on the MSM, therefore, the new method is very accurate, and can be generalized for other aspects. For example, we can design a non-Cartesian array. Also, the method is not a homogenization method but a far-field reconstruction method. Thus, we allow ourselves to preprocess the polarization currents distribution as we are not interested in the near field of the lens. In addition, a parametric study on the material and the unit cell size was performed. By testing the largest permittivity of the lens in a semi-infinite structure using the semi-infinite ASM, one can make a skillful decision about the permittivity of the cylinders and the unit cell size. While we could use the same parameters in a standard homogenization scheme with acceptable results, the use of the finite ASM as a complete design scheme gives better results and show a very good agreement with the continuous bulk flat lens far-field radiation patterns.

Appendix A
Semi-Infinite ASM

In this appendix, we formulate the method for a semi-infinite array. The geometry is the same as in Fig. 1(b); however, this time, we assume that the array is composed of a finite number N of layers of 1-D cylinder arrays with infinite number of cylinders in the x-direction (for a single layer demonstration, see Fig. 2). We assume that the polarization current distribution is known. The structure is excited with a PW $\mathbf{E}^{\text{inc}} = \exp\{-jk_0 y\}\widehat{z}$. Since the array is infinite in the x-direction, and the excitation is a PW with no phase progression in the x-direction, the spectrum amplitude of the scatterers in the same layer is the same for all the cylinders. Therefore, if the slab is realized with N layers, we have only N radii to extract. Let us consider a single layer of cylinders first. Again, since the excitation is a PW propagating in the y-direction, the physical problem in each unit cell is the same. The CW zero harmonic amplitude is υ [see in (2)]. We start with (9), however, that all of the equations in the matrix system are

$$\upsilon = 2\sum_{m=1}^{\infty} [\mathbf{S}]_m\, \upsilon + [\mathbf{B}]\, \upsilon \tag{19}$$

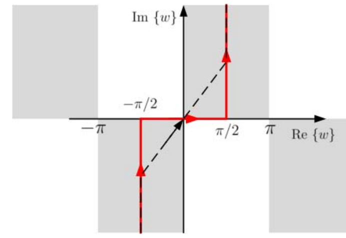

Fig. 13. Integration contour for the Sommerfeld representation of the Hankel function. The red line is the standard contour for observation angle $-\pi < \phi < \pi$. The black dashed line is a deformed contour used to ensure convergence of the sum in (22). The shaded areas are the valleys of the integrand.

where the $[\mathbf{B}]\upsilon$ term equals $-R_0(a,\epsilon_r)E^i(x, y = 0) = -R_0(a,\epsilon_r)$ from the same considerations as in Section II-B. $[\mathbf{S}]_m = -R_0(a,\epsilon_m)H_0^{(2)}(k_0 md)$, with d being the interelement distance. The sum is multiplied by 2, since the same summation has to be done to the right of the center cylinder and to its left. Using (6) in (19), we obtain

$$\upsilon = -2R_0(a,\epsilon_m)\upsilon\sum_{m=1}^{\infty} H_0^{(2)}(k_0 md) - R_0(a,\epsilon_m). \tag{20}$$

In order to simplify the summation, one can use the Sommerfeld integral given by [27]

$$H_0^{(2)}(k_0\rho) = \frac{1}{\pi}\int_{C_w} e^{-jk_0\rho\cos(w-\phi)}dw. \tag{21}$$

The contour C_w can be chosen with some arbitrariness; however, for our purpose, we use the red contour in Fig. 13. ϕ is the angle between the x-axis and the observation point given that the origin of the Hankel function is at the axis origin.

In the summation, ϕ takes on the value 0 if the cylinder we are summing is located to the left of the middle cylinder, or π if it is to the right. Similarly, in the summation, $\rho = md$. For convenience, let us sum the effect of the cylinders from the left. The summation becomes

$$\begin{aligned}\sum_{m=1}^{\infty} H_0^{(2)}(k_0 md) &= \sum_{m=1}^{\infty}\frac{1}{\pi}\int_{C_w} e^{-jk_0 md\cos w}dw\\ &= \frac{1}{\pi}\int_{C_w} e^{-jk_0 d\cos w}\sum_{m=0}^{\infty} e^{-jk_0 md\cos w}dw.\end{aligned} \tag{22}$$

Now, we have a geometric series inside the integral. Since the geometric series does not converge when w is on the real axis, we use the Cauchy theorem and deform the integration contour to the black dashed line in Fig. 13. On the new contour, the exponent obeys $|e^{-jk_0 md\cos\omega}| < 1$ for all ω values except $\omega = 0$. However, this point is a removable singularity and can be defined by the limit at that point. We define

$$\mathcal{L}_0 \triangleq \frac{1}{\pi}\int_{C_w}\frac{e^{-jk_0 d\cos w}}{1 - e^{-jk_0 d\cos w}}dw \tag{23}$$

which can be calculated numerically *apriori* to the calculation, since the unit cell size is well known.

In the layered structure, for each scatterer, there are layers above and/or below it. In order to add the effect of these layers, first, we find the field of a layer where each of its scatterers has zero harmonics υ_l

$$E_z^{\text{layer}} = \sum_{n=-\infty}^{\infty} \upsilon_l H_0^{(2)}(k_0\rho_n) \tag{24}$$

where $\rho_n = \sqrt{(x-x_n)^2+(y-y_n)^2}$, and $y_n = y_l$ is the constant over the entire layer. Next, we use the Sommerfeld representation of the Hankel function on the red contour in Fig. 13. Set $k_0^2 = k_x^2 + k_y^2$ (alternatively, $k_x = k_0 \cos w$ and $k_y = k_0 \sin w$), the red contour ensures that $\text{Re}\{k_y\} > 0$ and $\text{Im}\{k_x\} < 0$. Therefore. the PW representation of the Hankel is accurate for the half-plane $y > y_n$. We could set a contour to obtain the field in $y < y_n$ by choosing an alternative contour, and the results would be the same. We obtain

$$\begin{aligned} E_z^{\text{layer}} &= \sum_{n=-\infty}^{\infty} \upsilon_l \frac{1}{\pi} \int_{C_w} e^{-jk_0\rho_n \cos(w-\phi)} dw \\ &= \sum_{n=-\infty}^{\infty} \upsilon_l \frac{1}{\pi} \int_{-\infty}^{\infty} \frac{1}{k_y} e^{-jk_x(x-x_n)} e^{-jk_y(y-y_l)} dk_x \\ &= \frac{1}{\pi} \int_{-\infty}^{\infty} \upsilon_l \frac{e^{-jk_y(y-y_l)} e^{-jk_x x}}{k_y} \sum_{n=-\infty}^{\infty} e^{jk_x x_n} dk_x. \end{aligned} \tag{25}$$

In an equi-spaced layer, we have $x_n = nd$, and thus, we can use the Poisson summation formula [28]

$$\sum_{n=-\infty}^{\infty} e^{jk_x nd} = \frac{2\pi}{d} \sum_{n=-\infty}^{\infty} \delta\left(k_x - n\frac{2\pi}{d}\right) \tag{26}$$

where $\delta(k_x)$ is the Dirac's delta function. The delta function samples k_x at the points $k_{xn} = 2\pi n/d$. Since for our purpose, $d < \lambda_0$, we conclude that the only propagating contribution is for $n = 0$. That renders $k_{yn} = \sqrt{k_0^2 - k_{xn}^2} = k_0$. The evanescent contributors can be neglected. Equation (25) becomes

$$E_z^{\text{layer}} = \frac{2}{k_0 d} \upsilon_l e^{-jk_0(y-y_l)}. \tag{27}$$

From here, we can use (27) to represent the field that is incident on a specific cylinder as a result of a layer of cylinders above or below it. Consider that we have N layers above our scatterer of interest, and M layers below. The equation for this scatterer becomes

$$\begin{aligned} \upsilon_l = &-2R_0(a_l,\epsilon_m)\mathcal{L}_0\upsilon_l \\ &- \frac{2R_0(a_l,\epsilon_m)}{k_0 d} \sum_{n=1}^{N} \upsilon_n e^{-jk_0 nd} \\ &- \frac{2R_0(a_l,\epsilon_m)}{k_0 d} \sum_{m=1}^{M} \upsilon_m e^{-jk_0 md} \\ &- R_0(a,\epsilon_m) e^{-jk_0 y_l}. \end{aligned} \tag{28}$$

Again, set υ_n and υ_m according to the target spectrum, and we can extract a_l from the nonlinear equation using (13).

Appendix B
Standard Homogenization Technique Based on the MSM–the Infinite ASM

In this appendix, we formulate a conventional homogenization technique based on the MSM. It is conventional; in the sense, we assume that each cylinder is in an infinite array of cylinders identical to itself. Also, (1) is assumed to be correct at the macroscopic level. The array is excited by a PW $\mathbf{E}_z^{\text{inc}} = \exp\{-jk_0 y\}\hat{z}$. Under the previous assumption, the design does not depend on the excitation. The PW is chosen for the sake of convenience.

The main hypothesis here is that in any unit cell, the physical problem looks the same, with the exception of the phase of the incident field. From linearity, we obtain that any cylinder has the same zero cylindrical harmonic υ_0 multiplied by the phase of the incident field in the location of the cylinder. In order to formulate the method, we derive two equations. One connects υ_0 to the geometrical properties of the cylinders and referred to as the *microscopic equation*. The other connects υ_0 to the required effective permittivity and is called the *macroscopic equation*.

Let us begin with the microscopic equation. To this end, we use (28) from Appendix A and generalize it with the hypothesis. For now, assume a finite number L layers of cylinders above and below the central unit cell. We shall address the layers in pairs. The pairs are such that the distance from the central layer is equal. A layer with distance nd above the middle layer has, according to the hypothesis, a cylindrical harmonics $\upsilon_0 \exp\{-jk_0 nd\}$. The PW accumulates a phase of $\exp\{-jk_0 nd\}$ until it reaches the central unit cell, and therefore, the field from an upper layer is

$$E_z^{\text{up}} = \frac{2\upsilon_0}{k_0 d} e^{-2jk_0 nd} e^{jk_0 y}. \tag{29}$$

For a layer with distance nd below the middle layer, the cylindrical harmonics is $\upsilon_0 \exp\{jk_0 nd\}$, and the phase the PW accumulates is $\exp\{-jk_0 nd\}$. Therefore, the field is

$$E_z^{\text{down}} = \frac{2\upsilon_0}{k_0 d} e^{-jk_0 y}. \tag{30}$$

We obtain

$$\upsilon_0 = \frac{-R_0(a,\epsilon_m)}{1+2R_0(a,\epsilon_m)\mathcal{L}_0 + \frac{2}{k_0 d} R_0(a,\epsilon_m) \sum_{n=1}^{L} [1+e^{-2jk_0 nd}]}. \tag{31}$$

The summation does not converge when L goes to infinity, but it would not matter as we will see later on. Next, we derive the macroscopic equation, and its starting point is (1). The field E_z is averaged inside the unit cell. This average is composed from the averaged incident field and the average of the scattered field from all of the elements. The scattered field itself can be composed from the scattered field of the elements in the same layer and the field from the other layers. The averaged field of the incident field is

$$\left\langle E_z^{\text{inc}} \right\rangle = \frac{1}{d^2} \int_{-d/2}^{d/2} dx \int_{-d/2}^{d/2} e^{-jk_0 y} dy = \text{sinc}\left(\frac{k_0 d}{2}\right). \tag{32}$$

Next, we calculate the scattered field as a result of the entire layer the element belongs to. From (25) with (26), and including the evanescent modes, the field is

$$E_z^{\text{self}} = \frac{2\upsilon_0}{d}\sum_{n=-\infty}^{\infty}\frac{e^{-jk_{xn}x}e^{-jk_{yn}|y|}}{k_{yn}} \tag{33}$$

where $k_{xn} = 2\pi n/d$ and $k_{yn} = \sqrt{k_0^2 - k_{xn}^2}$. The average of this term is

$$\langle E_z^{\text{self}}\rangle = \frac{2\upsilon_0}{d}\sum_{n=-\infty}^{\infty}\frac{\operatorname{sinc}\left(\frac{k_{xn}d}{2}\right)\operatorname{sinc}\left(\frac{k_{yn}d}{4}\right)}{k_{yn}}e^{-j\frac{k_{yn}d}{4}}. \tag{34}$$

Note, that $k_{xn}d/2 = n\pi$, and therefore, $\operatorname{sinc}(k_{xn}d/2) = 0$ for all $n \neq 0$. We obtain

$$\langle E_z^{\text{self}}\rangle = \frac{2\upsilon_0}{k_0 d}\operatorname{sinc}\left(\frac{k_0 d}{4}\right)e^{-j\frac{k_0 d}{4}}. \tag{35}$$

For the other layers, combining (29) and (30), and averaging, we obtain for all the layers

$$\langle E_z^{\text{pair}}\rangle = \frac{2\upsilon_0}{k_0 d}\operatorname{sinc}\left(\frac{k_0 d}{2}\right)\sum_{n=1}^{\infty}[1 + e^{-2jk_0 nd}]. \tag{36}$$

Next, we set (32)-(36) in (1) to obtain

$$\upsilon_0 = \frac{A}{1 - B - \frac{2}{k_0 d}A\sum_{n=1}^{L}[1 + e^{-2jk_0 nd}]} \tag{37}$$

where

$$A = \frac{(k_0 d^2)}{4j}(\epsilon_r - 1)\operatorname{sinc}\left(\frac{k_0 d}{2}\right) \tag{38a}$$

$$B = \frac{k_0 d}{2j}(\epsilon_r - 1)\operatorname{sinc}\left(\frac{k_0 d}{4}\right)e^{-j\frac{k_0 d}{4}}. \tag{38b}$$

If we compare (37) to (12), we can take the summation terms out of the equation. From here, we set a target cylindrical harmonic with

$$\upsilon_0^{\text{target}} = \frac{A}{1 - B}. \tag{39}$$

The microscopic equation reduces to

$$\upsilon_0(a, \epsilon_m) = \frac{-R_0(a, \epsilon_m)}{1 + 2R_0(a, \epsilon_m)\mathcal{L}_0} \tag{40}$$

which is an analytic function of a. To extract the radius, we solve (13) as before.

This method is quite simple to apply and also quite efficient from the computational point of view. It is also as accurate as any other homogenization technique can get, as we used the MSM, which is very general. Therefore, this is a good candidate for comparison with the other methods.

References

[1] W. E. Kock, “Metallic delay lenses,” *Bell Syst. Tech. J.*, vol. 27, no. 1, pp. 58–82, Jan. 1948.

[2] A. Grbic and G. V. Eleftheriades, “Overcoming the diffraction limit with a planar left-handed transmission-line lens,” *Phys. Rev. Lett.*, vol. 92, no. 11, p. 117403, 2004.

[3] S. Enoch, G. Tayeb, P. Sabouroux, N. Guérin, and P. Vincent, “A metamaterial for directive emission,” *Phys. Rev. Lett.*, vol. 89, no. 21, p. 213902, 2002.

[4] A. K. Iyer and G. V. Eleftheriades, “A multilayer negative-refractive-index transmission-line (NRI-TL) metamaterial free-space lens at X-band,” *IEEE Trans. Antennas Propag.*, vol. 55, no. 10, pp. 2746–2753, Oct. 2007.

[5] Q. Wang *et al.*, “A broadband metasurface-based terahertz flat-lens array,” *Adv. Opt. Mater.*, vol. 3, no. 6, pp. 779–785, 2015.

[6] J. Zhang, Y. Luo, H. Chen, L. Ran, B.-L. Wu, and J. A. Kong. (2007). “Directive emission obtained by coordinate transformation.” [Online]. Available: https://arxiv.org/abs/0712.2755

[7] J. B. Pendry, D. Schurig, and D. R. Smith, “Controlling electromagnetic fields,” *Science*, vol. 312, pp. 1780–1782, Jun. 2006.

[8] W. X. Jiang, T. J. Cui, H. F. Ma, X. Y. Zhou, and Q. Cheng, “Cylindrical-to-plane-wave conversion via embedded optical transformation,” *Appl. Phys. Lett.*, vol. 92, no. 26, p. 261903, 2008.

[9] W. Tang, C. Argyropoulos, E. Kallos, W. Song, and Y. Hao, “Discrete coordinate transformation for designing all-dielectric flat antennas,” *IEEE Trans. Antennas Propag.*, vol. 58, no. 12, pp. 3795–3804, Dec. 2010.

[10] J. Brown, “Artificial dielectrics having refractive indices less than unity,” *Proc. IEE-IV, Inst. Monographs*, vol. 100, no. 5, pp. 51–62, 1953.

[11] H. T. Buscher, “Electrically controllable liquid artificial dielectric media,” *IEEE Trans. Microw. Theory Techn.*, vol. MTT-27, no. 5, pp. 540–545, May 1979.

[12] A. Dadgarpour, B. Zarghooni, B. S. Virdee, and T. A. Denidni, “Enhancement of tilted beam in elevation plane for planar end-fire antennas using artificial dielectric medium,” *IEEE Trans. Antennas Propag.*, vol. 63, no. 10, pp. 4540–4545, Oct. 2015.

[13] X. Liu, C. Lan, B. Li, Q. Zhao, and J. Zhou, “Dual band metamaterial perfect absorber based on artificial dielectric ‘molecules,’” *Sci. Rep.*, vol. 6, Jul. 2016, Art. no. 28906.

[14] R. E. Collin, *Field Theory of Guided Waves*. New York, NY, USA: McGraw-Hill, 1960.

[15] M. G. Silveirinha, “Generalized Lorentz–Lorenz formulas for microstructured materials,” *Phys. Rev. B, Condens. Matter*, vol. 76, no. 24, p. 245117, 2007.

[16] A. Alù, “First-principles homogenization theory for periodic metamaterials,” *Phys. Rev. B, Condens. Matter*, vol. 84, p. 075153, Aug. 2011.

[17] D. R. Smith and J. B. Pendry, “Homogenization of metamaterials by field averaging,” *J. Opt. Soc. Amer. B, Opt. Phys.*, vol. 23, no. 3, pp. 391–403, 2006.

[18] M. G. Silveirinha, “Metamaterial homogenization approach with application to the characterization of microstructured composites with negative parameters,” *Phys. Rev. B, Condens. Matter*, vol. 75, no. 11, p. 115104, 2007.

[19] M. G. Silveirinha, “Nonlocal homogenization model for a periodic array of ϵ-negative rods,” *Phys. Rev. E, Stat. Phys. Plasmas Fluids Relat. Interdiscip. Top.*, vol. 73, no. 4, p. 046612, 2006.

[20] J. J. Bonnefois, G. Guida, and A. Priou, “A new multiple scattering method application: Simulating an infinite 2D photonic crystal by analyzing, sorting and suppressing the border effects,” *Opt. Commun.*, vol. 251, no. 1, pp. 64–74, 2005.

[21] R. F. Harrington and J. L. Harrington, *Field Computation by Moment Methods*. London, U.K.: Oxford Univ. Press, 1996.

[22] R. Harrington, *Time-Harmonic Electromagnetic Fields*. Piscataway, NJ, USA: IEEE Press, 2001.

[23] T. F. Eibert, “A diagonalized multilevel fast multipole method with spherical harmonics expansion of the K-space Integrals,” *IEEE Trans. Antennas Propag.*, vol. 53, no. 2, pp. 814–817, Feb. 2005.

[24] P. P. Vaidyanathan, “Generalizations of the sampling theorem: Seven decades after Nyquist,” *IEEE Trans. Circuits Syst. I, Fundam. Theory Appl.*, vol. 48, no. 9, pp. 1094–1109, Sep. 2001.

[25] T. Grandke, “Interpolation algorithms for discrete Fourier transforms of weighted signals,” *IEEE Trans. Instrum. Meas.*, vol. IM-32, no. 2, pp. 350–355, Jun. 1983.

[26] J. Courtial and M. J. Padgett, "Performance of a cylindrical lens mode converter for producing Laguerre–Gaussian laser modes," *Opt. Commun.*, vol. 159, nos. 1–3, pp. 13–18, 1999.

[27] A. Sommerfeld, *Partial Differential Equations in Physics*, vol. 1. San Diego, CA, USA: Academic, 1949.

[28] E. M. Stein and G. Weiss, *Introduction to Fourier Analysis on Euclidean Spaces (PMS–32)*, vol. 32. Princeton, NJ, USA: Princeton Univ. Press, 2016.

Eran Falek (S'17) was born in Jerusalem, Israel, in 1981. He received the B.Sc. (*cum laude*) and M.Sc. degrees in electrical engineering from Ben-Gurion University of the Negev, Beer-Sheva, Israel, in 2010 and 2012, respectively, where he is currently pursuing the Ph.D. degree.

His current research interests include metamaterials, metasurfaces, and artificial dielectrics for antenna applications, multiple scattering, and antenna theory.

Reuven Shavit (M'82–SM'90) received the B.Sc. and M.Sc. degrees in electrical engineering from Technion–Israel Institute of Technology, Haifa, Israel, in 1971 and 1977, respectively, and the Ph.D. degree in electrical engineering from the University of California at Los Angeles, Los Angeles, CA, USA, in 1982.

From 1971 to 1993, he was a Staff Engineer and an Antenna Group Leader with Electronic Research Laboratories, Israeli Ministry of Defense, Tel Aviv, Israel, where he was involved in the design of reflector, microstrip, and slot antenna arrays. He was also a part-time Lecturer with Tel Aviv University, Tel Aviv, teaching various antenna and electromagnetic courses. From 1988 to 1990, he was associated with ESSCO, Concord, MA, USA, as a Principal Engineer, where he was involved in scattering analysis and tuning techniques of high-performance ground-based radomes. He is currently with the Ben-Gurion University of the Negev, Beer-Sheva, Israel, as a Professor, where he is involved in research in microwave components and antennas. His current research interests include metamaterials, smart antennas, tuning techniques for radomes, and numerical methods for design microstrip, slot, and reflector antennas.